Research Article

OPTICA

Room-temperature electroluminescence and light detection from III-V unipolar microLEDs without *p*-type doping

Bejoys Jacob,[1] Filipe Camarneiro,[1] Jérôme Borme,[2] José M. L. Figueiredo,[3] Jana B. Nieder,[1] and Bruno Romeira[1,*]

[1]INL—International Iberian Nanotechnology Laboratory, Ultrafast Bio- and Nanophotonics Group, Av. Mestre José Veiga s/n, 4715-330 Braga, Portugal
[2]INL—International Iberian Nanotechnology Laboratory, 2D Materials and Devices Group, Av. Mestre José Veiga s/n, 4715-330 Braga, Portugal
[3]Centra-Ciências and Departamento de Física, Faculdade de Ciências, Universidade de Lisboa, Campo Grande, 1749-016 Lisboa, Portugal
*bruno.romeira@inl.int

Received 17 October 2022; revised 31 January 2023; accepted 23 February 2023; published 20 April 2023

The twentieth-century semiconductor revolution began with "man-made crystals," or *p-n* junction-based heterostructures. This was the most significant step in the creation of light-emitting diodes (LEDs), lasers, and photodetectors. Nonetheless, advances where resistive *p*-type doping is completely avoided could pave the way for a new class of *n*-type optoelectronic emitters and detectors to mitigate the increase of contact resistance and optical losses in submicrometer devices, e.g., nanoLEDs and nanolasers. Here, we show that nanometric layers of AlAs/GaAs/AlAs forming a double-barrier quantum well (DBQW) arranged in an *n*-type unipolar micropillar LED can provide electroluminescence (EL) (emission at 806 nm from the active DBQW), photoresponse (responsivity of 0.56 A/W at 830 nm), and negative differential conductance (NDC) in a single device. Under the same forward bias, we show that enough holes are created in the DBQW to allow for radiative recombination without the need of *p*-type semiconductor-doped layers, as well as pronounced photocurrent generation due to the built-in electric field across the DBQW that separates the photogenerated charge carriers. Time-resolved EL reveals decay lifetimes of 4.9 ns, whereas photoresponse fall times of 250 ns are measured in the light-detecting process. The seamless integration of these multi-functions (EL, photoresponse, and NDC) in a single microdevice paves the way for compact, on-chip light-emitting and receiving circuits needed for imaging, sensing, signal processing, data communication, and neuromorphic computing applications.

https://doi.org/10.1364/OPTICA.476938

1. INTRODUCTION

The possibility of controlling the type and the level of conductivity of charge injection in *p-i-n* double heterostructures [1–5] was the seed for the semiconductor optoelectronics revolution [6]. To date, the heterostructure remains a ubiquitous element that is part of practically all optoelectronic devices. Despite the notable revolution made possible by the *p-i-n* architecture, in some materials *p*-type doping is not easily obtained, and in most cases, it adds cost and complexity to the material growth and device fabrication.

In organic materials, the use of an alternative *n-i-n* architecture in colloidal quantum dots showed advantages in simplifying the band alignment engineering [7,8]. In inorganic III-N materials, the *p*-type GaN contact remains a challenge in blue GaN LEDs (light-emitting diodes) [9,10], since it is difficult to grow and has low mobility for uniform carrier injection [11]. Strategies to mitigate this include the use of a unipolar (*n*-type) LED made of GaN on a Si substrate where holes are created by tunnel injection conduction [12]. In another approach, N-polar III-nitride tunnel junctions [13,14] eliminate the need of *p*-type doping in the contact layer but still require a thin (50–80 nm) *p*-type AlGaN layer to inject holes into the active region.

Notably, even in the case of III-V materials, where highly doped *p*-type contacts are easier to achieve, completely eliminating the *p*-type doping could bring enormous benefits. Specifically, with the recent miniaturization of III-V light-emitting and detector devices (e.g., micro- and nanoscale LEDs [15–17], nanolasers [18,19], and nanophotodetectors [20]), the use of resistive *p*-type doping play a crucial role on the devices' overall resistance and optical losses. To tackle this, the use of *n*-type-doped regions for carrier injection has been considered in either microscale vertical-cavity surface-emitting lasers with a buried low-resistance tunnel junction [21–23] or in nanolaser tunnel junctions [24]. Although these approaches have shown a reduction of the devices' resistance and a decrease of cavity losses, highly doped *p-n* junctions are still needed, which increase the internal optical losses and lead to nonthermal saturation of the output optical power [25]. To overcome this, recently, a few studies reflected upon the merits of exploiting unipolar, i.e., electron transporting, GaAs/AlGaAs [26]

and InGaAs/AlGaAs [27] heterostructures under strong electric fields for novel LEDs, but the required applied voltage (>50 V) makes these solutions impractical.

In a recent discovery, near-ultraviolet emission was demonstrated in cross-gap unipolar *n*-doped GaN/AlN double-barrier quantum well (DBQW) resonant tunneling heterostructures [28], also known as resonant tunneling diodes (RTD). Instead of using *p*-type doping and *p*-contacts, holes are created by direct interband tunneling in the GaN on the emitter side of the DBQW. This has been regarded as a major breakthrough in unipolar devices since the invention of the mid-infrared quantum cascade laser [29], creating expectations that electroluminescence (EL) could be observed in other unipolar *n-i-n* DBQW III-V materials covering a variety of wavelengths [30,31]. In a first noteworthy work in 2017, bistable EL at ∼870 nm was shown in a unipolar *n-i-n* GaAs-based DBQW [32], as a result of radiative recombination enabled by impact ionization in the collector region. In a more recent study, band-edge EL at ∼1631 nm was observed in the emitter-doped side of a unipolar *n-i-n* InGaAs DBQW device with $\approx 2 \times 10^{-5}$ external quantum efficiency [33], which was enabled by hole generation due to both Zener interband tunneling [28] and impact ionization [26] mechanisms. However, thus far, room-temperature EL from the intrinsic active DBQW material remains yet to be shown (similarly occurring in conventional *p-i-n* architectures). This has been observed only at low temperatures [34–37], while the dynamic properties of the emission remain totally unexplored.

In this work, we show that semiconductor nanometric layers of intrinsic AlAs/GaAs/AlAs forming a DBQW, arranged between collector and emitter *n*-type-doped GaAs layers, produce pronounced room-temperature near-infrared (NIR) EL from both the DBQW active region and the emitter-doped region. This architecture forms an *n*-type unipolar microLED without requiring *p*-type-doped layers for hole carrier transport. We estimate an internal quantum efficiency (IQE) of ∼0.23% at sub-mA current injection for micropillars with a diameter of ∼5 μm, which can be further improved by epilayer stack optimization [33] and surface passivation methods [38]. Here, impact ionization at low voltage [26] and possibly Zener interband tunneling at higher voltage [31] create holes in the high-field region on the collector and emitter sides of the DBQW, respectively. Holes are then transferred to the emitter side via resonant-tunneling (and other non-resonant mechanisms), thus providing radiative recombination in the DBQW region and in the emitter-doped side. Notably, the unipolar microLEDs show a noticeable photon absorption and photocurrent effect under NIR illumination (∼830 nm). This takes advantage of the light-excited electron-hole pairs locally separated in the DBQW [39,40]. As a result, under the identical forward direct current (DC) bias settings where light emission is observed, photodetection with a responsivity of ∼0.56 A/W at around 830 nm is obtained. Using time-correlated single photon counting and direct optical modulation measurements, we show that these photosensitive unipolar microLEDs can provide dynamic dual-functionality of emission and photodetection of high-speed modulated electrical and optical signals within a single device. We report decay times of the emission of ∼4.9 ns for the time-resolved EL and photoresponse fall times of ∼250 ns for the photocurrent, both cases under identical forward bias voltage conditions (∼3 V). Finally, we demonstrate that unipolar microLEDs with an embedded DBQW can provide an inherent region of negative differential conductance (NDC) [33,41,42], which could be exploited to support fast optical switching without requiring further electrical or optical components. The seamless integration of these multi-functions (EL, photodetection, and NDC) in a compact single device paves the way for low-cost light-emitting and optical receivers for transceiver circuits, self-clocking optical emitters for compact clock signal generation, and dense signal processing in photonic integrated circuits for data communication and neuromorphic applications.

2. DESIGN

The epilayer stack of the *n*-type (Si-doped) GaAs unipolar microLED was grown by molecular beam epitaxy (MBE) on a semi-insulating (SI) GaAs substrate. Figure 1(a) depicts a schematic of the unipolar microLED's semiconductor epilayer stack, including the DBQW intrinsic region. The DBQW [Fig. 1(a)] is formed by a stack of AlAs/GaAs/AlAs (3.1 nm/6 nm/3.1 nm) layers, surrounded by a GaAs layer of 10 nm (emitter spacer) and a 20-nm-thick layer (collector spacer), all of which are unintentionally doped. The cladding layers surrounding the active intrinsic region are obtained using a 100-nm-thick layer of $Al_{0.2}Ga_{0.8}As$ (doping concentration, $N_d = 2 \times 10^{16}$ cm^{-3}), followed by a 25-nm-thick layer of $Al_{0.2}Ga_{0.8}As$ ($N_d = 2 \times 10^{17}$ cm^{-3}), and a 25-nm-thick layer of $Al_{0.1}Ga_{0.9}As$ ($N_d = 2 \times 10^{17}$ cm^{-3}). These slightly *n*-doped-graded AlGaAs cladding layers were selected to enable the reduction of optical losses due to light absorption and to ensure that carriers are injected into and accumulated in the DBQW for efficient radiative recombination, similar to *p-i-n* architectures. Finally, the emitter bottom contact side consists of a 100-nm-thick layer of *n*-GaAs ($N_d = 2 \times 10^{17}$ cm^{-3}) and a 300-nm-thick layer of n^+-GaAs ($N_d = 2 \times 10^{18}$ cm^{-3}), while the collector top contact is composed of a 20 nm layer of *n*-GaAs ($N_d = 2 \times 10^{17}$ cm^{-3}) and a 20 nm layer of n^+-GaAs ($N_d = 2 \times 10^{18}$ cm^{-3}). We note that a thin (40 nm) stack of doped GaAs layers was selected for the collector top side to reduce the optical losses caused by light absorption, thus enabling more efficient light extraction.

Figure 1(b) shows a schematic of the energy band diagram of the unipolar microLED under applied voltage. The electrons flowing in the conduction band and injected into the quantum well recombine with minority holes that are created (radiative transitions $h\nu_{E1}$ and $h\nu_{LH1}$). We note that the holes are generated exactly in the DBQW active region where the radiative recombination occurs, instead of being injected from a *p*-type contact layer. The two main processes identified for hole generation include impact ionization (under low voltage) and Zener interband tunneling processes (under high voltage). At low voltage (moderate electrical field, <400 kV · cm^{-1}), holes are created across the collector region [see Fig. 1(b)] through the impact ionization process. At very high electric fields (>400 kV · cm^{-1}), additional holes are created in the emitter spacer. The schematic in Fig. 1(b) also depicts the spontaneous recombination processes that can occur in the spacer GaAs layer ($h\nu_{ES1}$) and in the *n*- and n^+-doped GaAs layers ($h\nu_{Eg}$) on the emitter side (and possibly on the collector side) [33]. For emission on the emitter side, holes are transported to the emitter by resonant tunneling (HH and LH) and other non-resonant mechanisms and recombine with free electrons that are abundant in these regions, especially in the *n*-doped GaAs layer.

Finally, Fig. 1(b) describes the formation of the electron-hole pairs (blue arrow) expected in unipolar microLEDs under illumination. These are generated by photon absorption processes

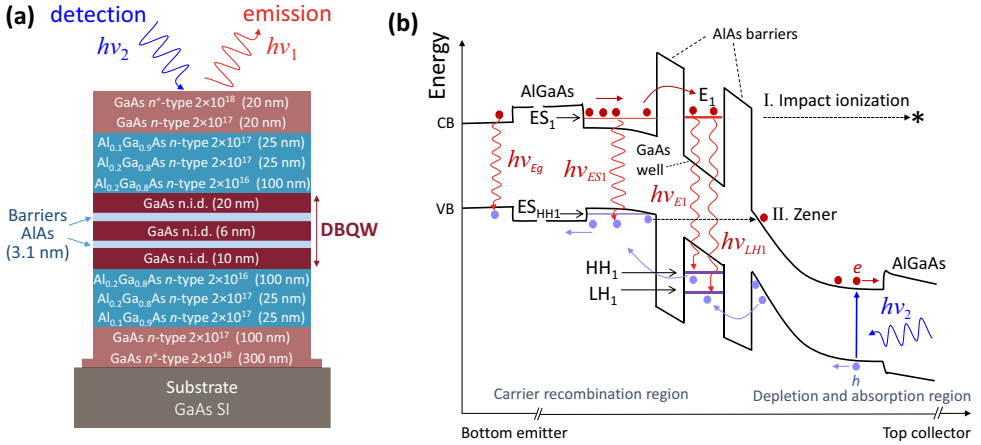

Fig. 1. Unipolar device semiconductor heterostructure. (a) The semiconductor epilayer stack grown by molecular beam epitaxy (MBE) on a semi-insulating (SI) GaAs substrate showing the intrinsic double-barrier quantum well (DBQW) active region. The design provides both emitting (hv_1) and detecting (hv_2) functions. (b) The schematic of the energy conduction (CB) and valence band (VB) diagram under applied voltage, along with the flow of charge (electrons, e, and holes, h) that enable light emission (red downward arrows) in the carrier recombination region and photon absorption (blue upward arrows) in the depletion region. The diagram shows a qualitative representation of the two main processes of electron-hole generation: I. impact ionization and II. Zener (interband) tunneling (HH, heavy hole; LH, light hole; ES, emitter spacer).

in the GaAs depletion and absorption regions in the collector spacer layer (20 nm). The local electric field in the depletion region provides a strong separation of photogenerated carriers, allowing the microLED device to function as a light-receiver. Photon absorption is also expected in the n-type-doped GaAs regions of the collector and emitter layers (not shown).

3. FABRICATION

Figure 2(a) illustrates a schematic diagram of a fabricated n-type unipolar microLED. The DBQW intrinsic region is depicted in the inset on the right side. The device consists of a micropillar with pillar widths (d) ranging from 5 μm < d < 9 μm, with both top (collector) and bottom (emitter) contacts using n^+-type doping. A dielectric material, in this case SiO_2, protects and isolates electrically the micropillar. To enable light-emitting and detection operations, a half-circle metal contact covers the top of the micropillar, providing light-out- (hv_1) and light-in- (hv_2) coupling from the top.

Unless stated otherwise, the microLEDs were fabricated by defining micropillars with electron beam lithography, which was followed by wet etching with a solution of $H_2SO_4 : H_2O_2 : H_20$ (1:2:20) until reaching the bottom GaAs-doped layer (etching of ~550 nm). The micropillars were then passivated with a thick layer (~650 nm) of SiO_2 and, via openings for the bottom and top contacts, which were defined by optical lithography using direct laser writing, followed by dry etching of the SiO_2. Both the top and bottom contacts (using a coplanar waveguide transmission line design) were formed using Ge/Ni/Au metal alloys. Finally, samples of fabricated devices were subjected to rapid thermal annealing at 400°C for 30 s (details of microfabrication are described in Supplement 1, Section S1). A scanning electron microscope (SEM) image of a representative fabricated microLED with a micropillar of ~9 μm diameter is shown in Fig. 2(b).

4. RESULTS

A. Room-Temperature Electroluminescence

In this work, microLEDs were measured at room-temperature and connected using a ground-signal-ground (GSG) coplanar waveguide electrical probe. The electrical DC bias was provided with a source meter connected to a bias-T. The EL was acquired using a fiber-based micro-electroluminescence (μEL) setup. The

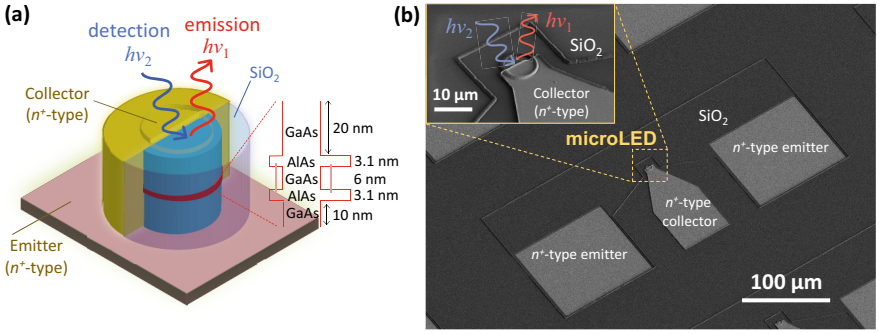

Fig. 2. Light-emitting and receiving unipolar microLED device. (a) The schematic diagram of the n-type microLED. The inset on the right side shows the energy band diagram of the AlAs/GaAs/AlAs double barrier quantum well (DBQW) region. (b) The scanning electron microscope (SEM) image of a fabricated unipolar microLED device with a micropillar of ~9 μm diameter. The inset shows a magnified image of the top micropillar half coated with the metal contact (n^+-type collector), enabling light in- and out-coupling.

EL from microLEDs was collected by a multimode lensed fiber (spot size ~25 μm) connected to a fiber-coupled spectrometer to acquire the optical spectra in the NIR region (details of the setup in Supplement 1, Section S2).

Figure 3(a) shows a typical EL spectra as a function of the bias current (for an applied voltage ranging from 2 to 3 V) for a representative microLED with 7-μm-pillar diameter (EL spectra for other diameters are given in Supplement 1, Section S3). As discussed, as a result of the high field achieved across the depletion region, the main mechanisms associated with hole generation in III-V *n*-type microLEDs include interband tunneling [28] and impact ionization [26]. However, considering the estimated electric field strength for the experimental voltage values used here ($<400\ \mathrm{kV \cdot cm^{-1}}$ up to 3 V, Supplement 1, Section S4), we attribute the main mechanism for hole generation in our devices to impact ionization. This results in pronounced radiative emission that can be described as follows. At moderate bias voltage ~1 V (after the turn-on, Fig. 4), electrons supplied by the emitter that cross the DBQW (by resonant tunneling or other pathways) are accelerated by the collector high electric field, gaining significant amount of energy, which leads to the generation of holes through impact ionization, creating (light and heavy) holes in the valence band of the collector region. Consequently, these electrons lose most of their energy, being available to recombine radiatively with the holes being generated, leading to EL. Under the influence of the collector electric field, a fraction of these holes will flow towards the collector barrier, eventually tunneling to the quantum well and leading to EL due to the recombination of electrons in the DBQW with the DBQW holes (both heavy and light holes). Another fraction of these holes accumulating in the collector barrier surroundings can go to the emitter region (through resonant tunneling or other non-resonant pathways), becoming available for radiative recombination with electrons either in the 10 nm emitter spacer quantum well (ESQW) or in the emitter doped region, producing the emission close to the GaAs band-edge transition.

As a result, we observe in the unipolar microLEDs four prominent EL emission signatures, Fig. 3, which are in agreement with the calculated interband transitions of our semiconductor layer stack [Fig. 1(b) and Supplement 1, Section S5]: (i) a pronounced peak ($h\nu_{E1} \sim 806$ nm) corresponding to the transition of an electron from the first energy level (E_1) in the conduction band of the DBQW to the heavy hole level (HH_1) in the valence band; (ii) a shoulder emission ($h\nu_{LH1} \sim 790$ nm), which corresponds to the transition of an electron from E_1 to the first energy level in the valence band for light holes (LH_1); (iii) a peak emission ($h\nu_{ES1} \sim 850$ nm) corresponding to the ESQW recombination of holes, which are transported by resonant tunneling to the emitter side with available electrons injected in the emitter spacer; and (iv) a broad peak, peaking at $h\nu_{Eg} \sim 861$ nm, which corresponds to the expected band-edge transition (E_g) at room-temperature from the GaAs bottom-doped layers in the emitter side.

As shown in Fig. 3(a), the relative intensity of the main emission peaks depends on the injection conditions. Under low current injection, the emission from the emitter side, $h\nu_{ES1} \sim 850$ nm, is dominant. As the pumping current increases, the emission from the quantum well (QW) active region ($h\nu_{E1} \sim 806$ nm) increases significantly. We attribute this to the efficient injection of electrons and holes into the QW. Similar EL spectral observations are made for all microLEDs measured with micropillar widths ranging from 5 to 9 μm (Supplement 1, Section S3). Figure 3(b) shows the EL of three different micropillar sizes under moderate pumping conditions. The emission from the DBQW, $h\nu_{ES1} \sim 806$ nm, is less pronounced for the smallest micropillar ($d = 5$ μm) than for the larger micropillars. We attribute this to the surface recombination effects of the etched GaAs micropillars, i.e., non-radiative recombination, which becomes more important as the pillars' surface-to-volume ratio increases [38]. Additional discussion on the relative intensity of the emission peaks is provided in Section 4.D.

Figure 4 shows the measured light-current-voltage (L-I-V) characteristics of a representative unipolar microLED. The I-V exhibits a diode-like turn-on voltage of ~1 V, and the L-I shows a monotonous increase of emission within the measured current range. Because of the small contact area of the devices considered here, a large current density (up to $3\ \mathrm{kA \cdot cm^{-2}}$) is obtained. The devices exhibit a large series resistance (~2.47 kΩ) that is partially related to the small contact area of the micropillar device, the contribution from the AlGaAs layers, the non-homogenous wet etching, and due to non-optimized metal contacts. The measured L-I-Vs for additional microLEDs ranging from 7 to 9 μm (Supplement 1, Section S6) show similar characteristics. Since the devices are based on a DBQW configuration, negative differential conductance (NDC) signatures from these microLEDs can also

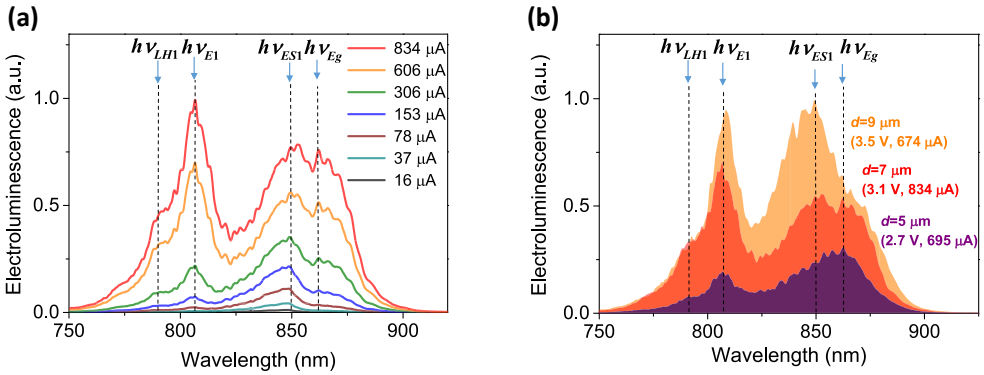

Fig. 3. Electroluminescence (EL) at room-temperature. (a) The EL spectra as a function of the pumping current (voltage ranging from 2 to 3 V) for a 7-μm-wide pillar microLED. On top are marked the emission peaks $h\nu_{E1}$, $h\nu_{LH1}$, $h\nu_{ES1}$, and $h\nu_{Eg}$, see Fig. 1(b). The wavelength of the observed peaks are almost independent of the current injection (and voltage). For the range of the current levels analyzed here, only a small red shift of ~1 nm was observed for the emission from the DBQW while the other peaks were red shifted within ~3 nm. (b) The EL for the microLEDs as a function of the micropillar width ($d = 5$ μm, 7 μm and 9 μm) and at pumping conditions >500 μA (>2.7 V).

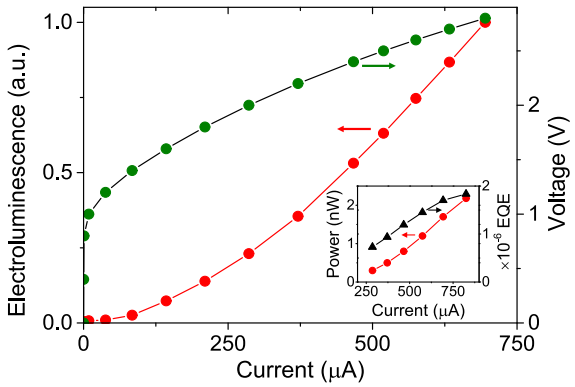

Fig. 4. Static characteristics. Light-current-voltage (L-I-V) characteristics of a 5 μm wide pillar unipolar microLED. The inset shows the collected optical power output (P_{out}) from the microLED as a function of the current and the external quantum efficiency (EQE).

be expected. For these devices, non-resonant current pathways seem to dominate resulting, in no clear observation of reproducible NDC. Nonetheless, signatures of NDC were observed for larger area devices with improved fabrication methods (and this is discussed in Section 4.D, Fig. 7).

The inset of Fig. 4 shows the power-current ($P-I$) characteristic and the external quantum efficiency (EQE) for the same device. The optical power was measured using a calibrated fiber-coupled optical power meter (details of the setup in Supplement 1, Section S2), and is calculated as

$$\mathrm{EQE} = \frac{e\,P_{\mathrm{out}}}{I_E h\nu}, \tag{1}$$

where P_{out} is the measured output power, and I_E is the terminal electric current measured across the microLED. The low EQE value ($\approx 10^{-6}$) reported here is mainly attributed to the inefficient light extraction efficiency ($\sim$0.02) from the high index semiconductor, which leads to the low coupling efficiency (η_c) of light to the lensed fiber with a small numerical aperture (NA). The coupling efficiency [33] is given by

$$\eta_c \approx \frac{1}{4}\left(\frac{\mathrm{NA}}{n}\right)^2. \tag{2}$$

The internal quantum efficiency (IQE) is obtained based on the relation

$$\mathrm{EQE} = \eta_c \mathrm{IQE}. \tag{3}$$

Considering the refractive index of the GaAs layer $n \approx 3.55$ (for $\lambda \sim 800-870$ nm) and the NA ~ 0.2 for the lensed fiber, we estimate a coupling efficiency of $\eta_c = 7.93 \times 10^{-4}$, resulting in an internal quantum efficiency (IQE) of $\sim 2.3 \times 10^{-3}$ at the maximum applied bias reported here.

The IQE in inorganic p-i-n-type microLEDs (III-V or III-N such as GaN- and AlGaInP-based LEDs) depends on the LED size [43], due to leakage current and/or nonradiative recombination effects (surface related) caused by sidewall defects in smaller chip geometries [44–46]. The unipolar microLEDs reported here can show EQE values more equivalent to other inorganic LEDs when the materials and sizes (<10 μm) considered are similar. In Supplement 1, Section S7, we analyze the factors for the efficiency values reported here. Neglecting leakage or carrier injection effects, our studies reveal that the IQE can be substantially improved (IQE $\sim$ 0.3, Fig. S8) using surface passivation treatments reported elsewhere for the GaAs materials [38], which are able to suppress non-radiative effects in the micropillars. Another factor that plays a role in the IQE is the carrier injection efficiency (estimated $\sim$0.11, Supplement 1, Section S7). The injection efficiency in our unipolar microLEDs is strongly dependent on the electric field across the DBQW, since holes are generated by impact ionization and Zener tunneling, mechanisms which are considerably different from the p-i-n-type LED architecture. Optimization of the epilayer structure (namely the DBQW, the depletion region, and the cladding layers [33]) to increase the electric field across the device can provide improvements of hole-generation mechanism via the interband-tunneling and impact-ionization mechanisms. In perspective, considering a few practical improvements (see Supplement 1, Section S7), including a 14-fold improvement of radiative efficiency via surface passivation [38], a 2-fold increase in carrier injection efficiency in a higher electric field device [33], and a 5-fold increase in light extraction efficiency via nanostructuring of the GaAs material [47], could increase EQE $> 10^{-4}$ (Fig. S9) in unipolar microLEDs without significantly changing our current design. This is only 2–3 orders of magnitude lower than the EQEs reported in inorganic p-i-n-type microLEDs of comparable sizes (<10 μm) and III-V-based materials [43].

B. Static Photoresponse Characteristics

The photoresponse characteristics of the unipolar microLEDs were measured using a similar fiber-based setup as used to collect the EL. However, in this case, light from a continuous wave (CW) fiber-coupled laser source was used to excite the microLED and coupled into the micropillar using a lensed fiber (Supplement 1, Section S2). Figure 5(a) shows the typical photoresponse characteristic for the microLED with a 5 μm diameter under identical forward DC bias conditions (2.8 V) where EL was observed. When illuminated with an optical power $\sim$6 mW at around 830 nm, a significant photocurrent is measured (dashed blue line, dark current plus photocurrent). We note light is mostly absorbed in the depleted GaAs spacer layer [Fig. 1(b)], providing the generation of electron-hole pairs. The local built-in electric field is enhanced by the applied voltage across the DBQW, which enables efficient separation of photogenerated charge carriers and results in a large photocurrent effect [inset of Fig. 5(a)]. As also shown in the inset of Fig. 5(a), the photocurrent begins to saturate at higher incident light pumping conditions (>4 mW). The corresponding photocurrent is given by

$$\Delta I_P(V) = I_P(V) - I_{\mathrm{dark}}(V), \tag{4}$$

where I_P represents the current observed after light injection with a laser power, P, into the microLED. The parameter I_{dark} represents the current under dark conditions (no illumination with laser). The responsivity ($\Re$) is estimated by the ratio of the photocurrent (ΔI_p) to the effective optical power input (P_{eff}) coupled to the microLED for a given bias condition (V),

$$\Re(V) = \frac{\Delta I_P(V)}{P_{\mathrm{eff}}}, \tag{5}$$

where

$$P_{\mathrm{eff}} = P\left(\frac{A_{\mathrm{mesa}}}{A_{\mathrm{spot}}}\right). \tag{6}$$

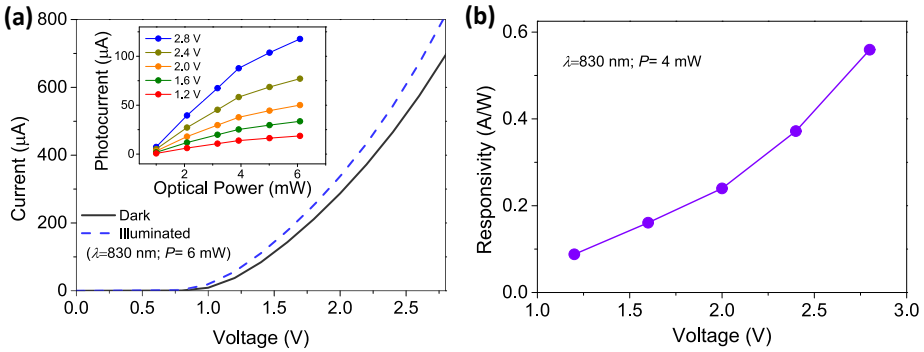

Fig. 5. Photoresponse characteristics. (a) Dark (black solid line) and illuminated (blue dashed line) current-voltage (I-V) traces of the photosensitive microLED. Here, a 6 mW CW laser operating at around 830 nm was used to illuminate a 5-μm-wide pillar microLED. The photocurrent is shown in the inset as a function of the laser optical power, P, for the increasing bias voltage. (b) Responsivity, using Eq. (5), as a function of the applied voltage for the following illumination conditions: 4 mW CW laser power operating at 830 nm.

A_{mesa} is the area of the microLED, and A_{spot} is the size of the laser spot incident into the microLED. The diameter of the laser spot at the working distance of the lensed fiber is estimated to be ∼25 μm. Figure 5(b) shows the responsivity when illuminated with a laser input power of ∼4 mW operating at λ ∼ 830 nm. The responsivity increases from ∼0.09 A/W (voltage of 1.2 V) up to ∼0.56 A/W (voltage of 2.8 V). Note that in our calculations we have neglected additional optical losses due to the light reflection in the air-semiconductor interface of the microLED devices.

C. Dynamic Response of Unipolar MicroLEDs

1. Emitter: Optical Dynamic Response

Time-resolved EL measurements were used to estimate the lifetimes of the NIR emission of the unipolar microLEDs. As depicted in Fig. 6(a), microLEDs were electrically driven by square-wave voltage pulses (peak to peak voltage, $V_{pp} = 1$ V; pulse width, $t_{in} = 100$ ns) using a pulse generator connected to the radio frequency (RF) port of a high-bandwidth bias-T (0.1–4200 MHz) and DC biased through a source meter (detailed description of the setup in Supplement 1, Section S8). The optical signal from the microLED was collected by a lensed fiber (as described for the static characterization) and coupled to a single-photon counting avalanche photodetector (APD). The APD was connected to a correlation card controller. The controller correlates the photon arrival times at the APD (start signal) with the pulse generator's signal arrival times (stop signal) in order to measure the time-resolved EL. A histogram of the arrival times is then constructed corresponding to the time-dependent output intensity of the electrically modulated microLEDs. The time-resolved EL obtained as a function of the bias voltage is given in Fig. 6(b), showing a longer determined decay lifetime (τ) with increasing forward bias voltage. For lifetime fitting, a single exponential fit was used (using Origin software). Clearly, the spontaneous emission process dominates at higher pumping conditions, as evidenced by the long decay lifetime of ∼4.9 ns [panel (iii)]. This limits the microLED frequency response to a 3-dB modulation bandwidth of ∼30 MHz ($f_{3\,\text{dB,emitter}} \approx 1/(2\pi\tau)$. The shorter decay lifetimes (∼1−2 ns) at lower bias [panels (i) and (ii)] indicate that non-radiative recombination processes, in particular surface recombination, have a significant influence on shortening the decay time. These short lifetimes have been observed in time-resolved photoluminescence (TRPL) measurements in micropillars of similar materials [38]. Although the efficiency of the microLEDs can be limited by such non-radiative surface-related processes, this characteristic leads to the possibility of operating at modulation bandwidths beyond the limitations of the slow radiative recombination process. We note, however, that the on-switching of the microLED is slower since it is still limited by the radiative processes, which has an impact in the overall on-off modulation cycle.

2. Receiver: Photocurrent Dynamic Response

To characterize the capability of the microLEDs of working as a receiver, Fig. 6(c), devices were illuminated by a laser (λ ∼ 830 nm, $P \sim 3.2$ mW). The laser was driven by square electrical pulsed signals with a voltage (V_{pp}) of 1 V and $t_{in} = 2$ μs and provided by a signal generator via the laser driver controller. The photoresponse in time from the microLEDs was then measured through the RF port of the bias-T connected to an oscilloscope (Supplement 1, Section S9). Figure 6(d) shows the photocurrent response in the time-domain as a function of the applied voltage. The photoresponse fall time (defined as the time between drop in photocurrent from 90% to 10% of its maximum value) varied from a long response time of ∼660 ns at lower bias voltage (2 V), up to ∼250 ns under higher bias voltage conditions (3.5 V). The photoresponse rise times were also recorded (typically ∼270 ns at 3.5 V), showing identical magnitude as the fall time. We calculated the modulation bandwidth, $f_{3\,\text{dB,detector}} = 0.7/(\tau_r + \tau_f)$ [48], where τ_r is the rise time and τ_f is the fall time of the photocurrent response and obtained a cut-off frequency of ∼1.3 MHz when the device is biased at 3.5 V [Fig. 6(d)(iii)]. We note this modulation speed is lower than the modulation bandwidth of ∼30 MHz for the microLED emitter operation. We attribute this to the dynamic photoresponse related to the slow diffusion of carriers (holes) photogenerated in other GaAs-doped layers other than the depleted GaAs intrinsic layer. Improvements of the modulation speed could be obtained, for example, by selecting non-absorbing top- and bottom-doped contact layers in the NIR range of operation or by removing the top and bottom GaAs layers by etching during the fabrication process.

D. Toward Negative Differential Conductance

To achieve NDC from the I-V characteristic, a key property of DBQW-based devices, from the same epilayer stack [Fig. 1(a)]

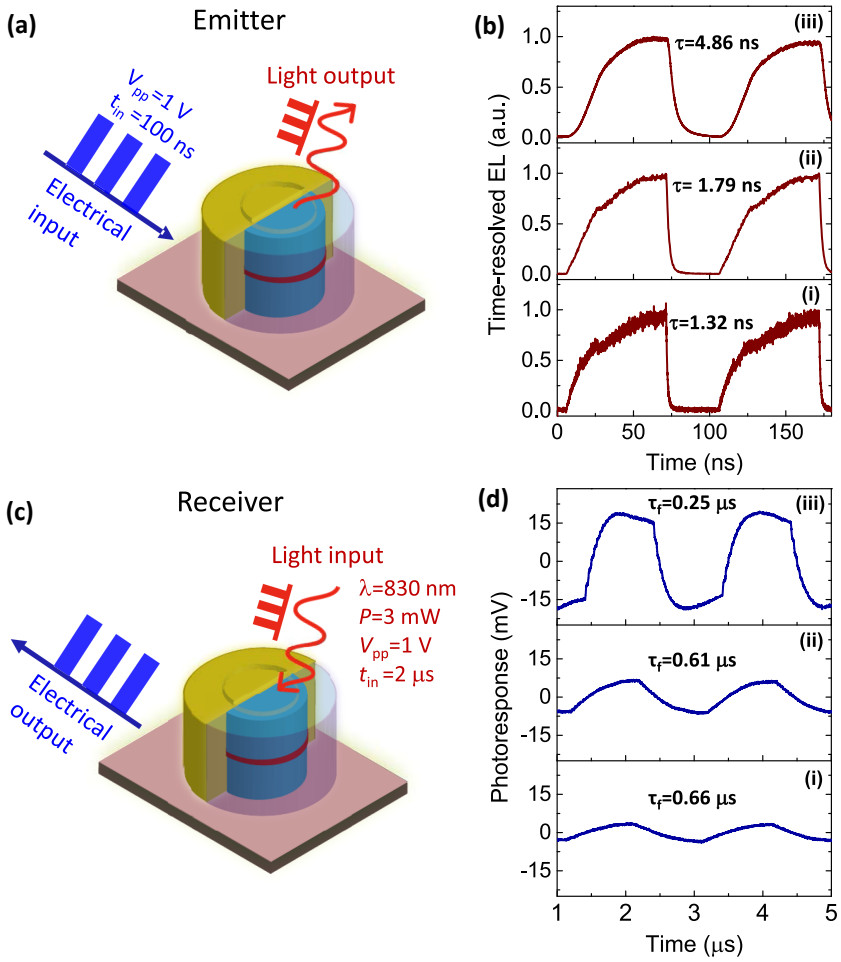

Fig. 6. Temporal electrical and optical response of the microLED. (a) The emitter configuration for electro-optical modulation. (b) The time-resolved electroluminescence (EL) as a function of the forward bias voltage: (i) 2 V, (ii) 2.5 V, and (iii) 3 V for 1 V, 100 ns input electrical pulses. The determined decay lifetime (τ) is indicated for each bias condition. (c) The receiver configuration for opto-electrical modulation. (d) The photocurrent response to illumination by a laser source ($\lambda \sim 830$ nm) driven by 1 V, 2 μs square-wave voltage pulses. The photocurrent was measured as a function of the forward bias voltage: (i) 2 V, (ii) 2.6 V, and (iii) 3.5 V. The photoresponse fall time time (τ_f) indicated for each bias condition is determined as the time between 10% and 90% of the maximum photocurrent.

another fabrication run of samples was implemented to obtain larger area ($d \sim 20$ μm) microLED devices (See Supplement 1, Section S1). Here, an improved passivation method was used employing Si_xN_y deposition by low-frequency plasma-enhanced chemical vapor deposition (PECVD) [38]. From the fabricated microLEDs, we have observed reproducible signatures of NDC in the I-V characteristics [Fig. 7(a)]. We have obtained a peak current ($I_p = 298$ μA) at $V_p = 2.67$ V and a valley current ($I_v = 284$ μA) at $V_v = 2.8$ V. The peak-to-valley-current ratio (PVCR) is 1.03 and a window of NDC of $\Delta V = V_v - V_p$. The microLED devices also showed EL at room-temperature (here collected from the lateral side of the micropillar) with emission signatures from both the DBQW active region and the GaAs band-edge transition, identical to the microLED devices (5 μm $< d <$ 9 μm) reported in Section 4.A.

Figure 7(b) shows the ratio of the maximum EL counts per second recorded from the quantum well emission (L_{QW}) to the emission from the GaAs emitter regions (L_{Bulk}), as a function of the bias voltage. We note that the overall EL spectra monotonously increases with the bias voltage, as shown in the inset of Fig. 7(b), at the peak and the valley voltage. However, the emission ratio L_{QW}/L_{Bulk} exhibits a non-linear behavior. First, L_{QW}/L_{Bulk} increases well above one until just before V_p, indicating that before the peak voltage (maximum overlap of the QW resonance with the Fermi energy distribution), the L_{QW} emission dominates. Then the L_{QW}/L_{Bulk} ratio starts to decrease as the bias continues to rise, indicating that the L_{Bulk} emission on the emitter side becomes predominant. Interestingly, $L_{QW}/L_{Bulk} \sim 1$ when the current value at the V_c voltage is the same as the peak current, I_p. We attribute this non-linear behavior to the interplay between the resonant tunneling and the non-resonant current components. Considering the range of applied bias within the NDC, we can assume a constant hole generation rate and that in principle, holes have several channels to be transported either to the QW or to the emitter, e.g., through the LH and HH resonant levels and other off-resonance mechanisms. However, the electron concentration in the quantum well is controlled by the applied voltage across the DBQW. As a result, beyond the peak voltage, an increase in the bias voltage leads to a reduction of the electron concentration in the well, resulting in a reduction of the QW EL, thus explaining the reduction of the L_{QW}/L_{Bulk} ratio. In fact, that reduction should start slightly before the current peak (I_p) is reached, as observed

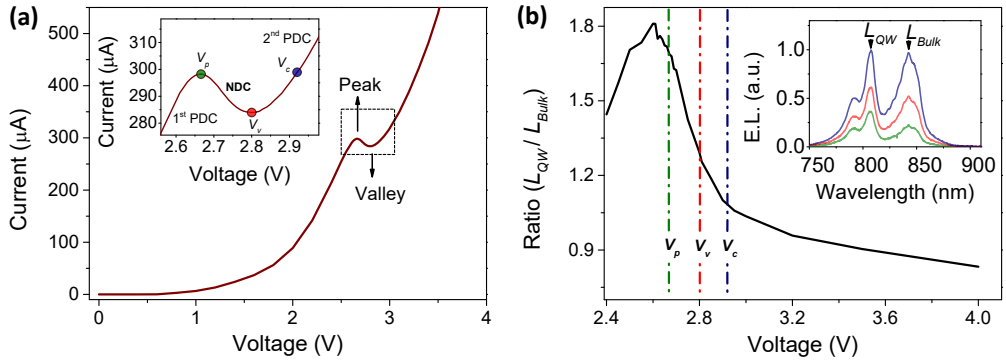

Fig. 7. Negative differential conductance (NDC) and electroluminescence (EL). (a) The current-voltage (I-V) characteristic of a unipolar microLED ($d \sim 20$ μm) showing the regions of NDC and positive differential conductance (PDC). The inset shows a magnified plot of the NDC region. The peak voltage (V_p), valley voltage (V_v), and V_c (bias current point identical to I_p) are marked as green, red, and blue dots, respectively. (b) The ratio of the maximum EL counts per second in the quantum well (L_{QW}) to the GaAs emitter regions (L_{Bulk}), as a function of the bias voltage. The dashed vertical lines mark the V_p (green), V_v (red), and V_c (blue). The inset shows the EL spectra in the peak (green), valley (red), and V_c (blue) bias voltage conditions.

in Fig. 7(b). This is because the resonant component of the current reaches its maximum slightly before the current peaks, since initially the resonant current drop is compensated by the steady increase of the non-resonant current, and only then does the resonant current reduction becomes significant to give rise to the NDC region.

The simultaneous observation of NDC and EL control from this unipolar microLED opens up the possibility of further optimizing the epilayer design to achieve much larger PVCR values, which could support optical switching or optical oscillations in a single LED device without requiring further electronic or optoelectronic components [42].

5. CONCLUSION

We have demonstrated for the first time, to the best of our knowledge, that the active AlAs/GaAs/AlAs double-barrier quantum well (DBQW) material of a unipolar (electron transporting) *n-i-n* microLED emits pronounced room-temperature radiative spontaneous light emission at 806 nm. We note that all prior reports of emission at room-temperature from GaAs, InP, or GaN DBQW-based devices were observed from the doped bulk GaAs layers next to the contacts and not from the active DBQW intrinsic region (similar to conventional *p-i-n* architectures). This achievement is of key importance, since several of the design strategies employed in *p-i-n*-type LEDs could be used to improve the optical and electrical properties of *n*-type unipolar LEDs. Importantly, the design of the active DBQW nanostructure can be used to control the optical emission properties, e.g., wavelength tuning, of unipolar LEDs.

Using this unique architecture, we show in a single unipolar microLED device: (i) room-temperature near-infrared (NIR) electroluminescence from the DBQW embedded active region, (ii) NIR light emission and light detection using the same forward bias conditions; (iii) first studies on the dynamic properties of the emission and demonstration of light-transmission and light-receiving operations of modulated signals at nanosecond speeds; and (iv) demonstration of negative differential conductance (NDC) in the current-voltage characteristic, a key property in DBQW-based devices.

Since highly doped *p*-type layers are fully avoided, this novel microdevice can potentially be scaled down to sub-μm sizes, e.g., nanoLEDs or nanolasers, while mitigating high electrical contact resistance and optical absorption losses associated with *p*-type doped materials. This significantly reduces the cost and simplifies the heterostructure band engineering typically required in *p-i-n* devices and could be, in principle, extended to other III-V compound material systems, e.g., InGaAs/InP, covering a wide-range of wavelengths for a new class of *n*-type nano-optoelectronic devices. Notably, photodetection with a responsivity of 0.56 A/W at 830 nm is obtained under identical forward DC bias settings where light emission is observed. This dual-capability was used to achieve either light-transmission or light-receiving of signals at nanosecond speeds, bringing to light a new class of optoelectronic devices for electro-optical and opto-electrical modulation configurations.

Importantly, we have demonstrated the possibility of achieving simultaneous electroluminescence and NDC. A result that can be explored in the fabrication of compact optoelectronic oscillator circuits or other nonlinear circuitry. This microdevice with seamless integrated multi-capabilities (electroluminescence, photoresponse and NDC) could find applications in low-cost large-array transceiver circuits to implement dense signal processing and optical clocking functions in photonic integrated circuits, as well as in energy-efficient data communication, signal processing, and sensor computing systems for edge computing applications. The observation of NDC from these devices also opens up the possibility of applying these devices in high-speed integrated emitting-detecting non-linear units for neuromorphic photonic computing applications.

Funding. European Union, HORIZON EUROPE Framework Programme, Project 828841 – ChipAI, and Project 101046790 – InsectNeuroNano.

Acknowledgment. We acknowledge access and support by the Micro and Nanofabrication Facility and the Nanophotonics and Bioimaging Facility at INL. We also acknowledge Qusay Raghib Ali Al-Taai, Jue Wang, and Edward Wasige of the University of Glasgow for the annealing of samples and the discussions of the design of the coplanar waveguide transmission line-based electrical contacts. BJ acknowledges the support of the work in frame of the PhD program in Electrical Engineering, Electronics and Automation at Carlos III University of Madrid, Department of Electronic Technology, Group of Displays and Photonic Applications, Avda de la Universidad, 30, 28911, Leganes, Madrid, Spain.

Disclosures. The authors declare no conflicts of interest.

Data availability. Data underlying the presented results may be obtained from the authors upon reasonable request.

Supplemental document. See Supplement 1 for supporting content.

REFERENCES

1. D. N. Nasledov, A. A. Rogachev, S. M. Ryvkin, and B. V. Tsarenkov, "Recombination radiation of galium arsenic," Sov. Phys. Solid State **4**, 782–784 (1962).
2. N. Holonyak, Jr. and S. F. Bevacqua, "Coherent (visible) light emission from Ga($As_{1-x}P_x$) junctions," Appl. Phys. Lett. **1**, 82–83 (1962).
3. M. I. Nathan, W. P. Dumke, G. Burns, F. H. Dill, and G. Lasher, "Stimulated emission of radiation from GaAs *p-n* junctions," Appl. Phys. Lett. **1**, 62–64 (1962).
4. T. M. Quist, R. H. Rediker, R. J. Keyes, W. E. Krag, B. Lax, A. L. McWhorter, and H. J. Zeigler, "Semiconductor maser of GaAs," Appl. Phys. Lett. **1**, 91–92 (1962).
5. H. Kroemer, "A proposed class of hetero-junction injection lasers," Proc. IEEE **51**, 1782–1783 (1963).
6. Z. Alferov, "Heterostructures for optoelectronics: history and modern trends," Proc. IEEE **101**, 2176–2182 (2013).
7. R. M. R. Adão, T. Sun, B. Romeira, P. Alpuim, and J. B. Nieder, "Spectral-temporal luminescence properties of colloidal CdSe/ZnS quantum dots in relevant polymer matrices for integration in low turn-on voltage AC-driven LEDs," Opt. Express **30**, 10563–10572 (2022).
8. V. Wood, M. J. Panzer, J.-M. Caruge, J. E. Halpert, M. G. Bawendi, and V. Bulović, "Air-stable operation of transparent, colloidal quantum dot based LEDs with a unipolar device architecture," Nano Lett. **10**, 24–29 (2010).
9. S. Nakamura, M. Senoh, and T. Mukai, "High-power InGaN/GaN double-heterostructure violet light emitting diodes," Appl. Phys. Lett. **62**, 2390–2392 (1993).
10. S. Nakamura, T. Mukai, and M. Senoh, "High-power GaN P-N junction blue-light-emitting diodes," Jpn. J. Appl. Phys. **30**, L1998–L2001 (1991).
11. H. Amano, M. Kito, K. Hiramatsu, and I. Akasaki, "P-Type conduction in Mg-doped GaN treated with low-energy electron beam irradiation (LEEBI)," Jpn. J. Appl. Phys. **28**, L2112–L2114 (1989).
12. M. A. Zimmler, J. Bao, I. Shalish, W. Yi, V. Narayanamurti, and F. Capasso, "A two-colour heterojunction unipolar nanowire light-emitting diode by tunnel injection," Nanotechnology **18**, 395201 (2007).
13. H. Jia, H. Yu, Y. Kang, Z. Ren, M. H. Memon, W. Guo, H. Sun, and S. Long, "Investigation of quantum structure in N-polar deep-ultraviolet light-emitting diodes," J. Appl. Phys. **129**, 133102 (2021).
14. Y. Zhang, G. Deng, Y. Yu, Y. Wang, D. Zhao, Z. Shi, B. Zhang, and X. Li, "Demonstration of N-polar III-nitride tunnel junction LED," ACS Photon. **7**, 1723–1728 (2020).
15. V. Dolores-Calzadilla, B. Romeira, F. Pagliano, S. Birindelli, A. Higuera-Rodriguez, P. J. van Veldhoven, M. K. Smit, A. Fiore, and D. Heiss, "Waveguide-coupled nanopillar metal-cavity light-emitting diodes on silicon," Nat. Commun. **8**, 14323 (2017).
16. G. Shambat, B. Ellis, A. Majumdar, J. Petykiewicz, M. A. Mayer, T. Sarmiento, J. Harris, E. E. Haller, and J. Vučković, "Ultrafast direct modulation of a single-mode photonic crystal nanocavity light-emitting diode," Nat. Commun. **2**, 539 (2011).
17. K. C. Y. Huang, M.-K. Seo, T. Sarmiento, Y. Huo, J. S. Harris, and M. L. Brongersma, "Electrically driven subwavelength optical nanocircuits," Nat. Photonics **8**, 244–249 (2014).
18. G. Crosnier, D. Sanchez, S. Bouchoule, P. Monnier, G. Beaudoin, I. Sagnes, R. Raj, and F. Raineri, "Hybrid indium phosphide-on-silicon nanolaser diode," Nat. Photonics **11**, 297–300 (2017).
19. B. Ellis, M. A. Mayer, G. Shambat, T. Sarmiento, J. Harris, E. E. Haller, and J. Vučković, "Ultralow-threshold electrically pumped quantum-dot photonic-crystal nanocavity laser," Nat. Photonics **5**, 297–300 (2011).
20. P. Wen, P. Tiwari, S. Mauthe, H. Schmid, M. Sousa, M. Scherrer, M. Baumann, B. I. Bitachon, J. Leuthold, B. Gotsmann, and K. E. Moselund, "Waveguide coupled III-V photodiodes monolithically integrated on Si," Nat. Commun. **13**, 909 (2022).
21. S. Spiga, W. Soenen, A. Andrejew, D. M. Schoke, X. Yin, J. Bauwelinck, G. Boehm, and M.-C. Amann, "Single-mode high-speed 1.5-μm VCSELs," J. Lightwave Technol. **35**, 727–733 (2017).
22. M. Ortsiefer, R. Shau, G. Böhm, F. Köhler, G. Abstreiter, and M.-C. Amann, "Low-resistance InGa(Al)As tunnel junctions for long wavelength vertical-cavity surface-emitting lasers," Jpn. J. Appl. Phys. **39**, 1727–1729 (2000).
23. W. Hofmann, "High-speed buried tunnel junction vertical-cavity surface-emitting lasers," IEEE Photon. J. **2**, 802–815 (2010).
24. C.-Y. Fang, S. H. Pan, F. Vallini, A. Tukiainen, J. Lyytikäinen, G. Nylund, B. Kanté, M. Guina, A. El Amili, and Y. Fainman, "Lasing action in low-resistance nanolasers based on tunnel junctions," Opt. Lett. **44**, 3669–3672 (2019).
25. O. S. Soboleva, V. V. Zolotarev, V. S. Golovin, S. O. Slipchenko, and N. A. Pikhtin, "The effect of the carrier drift velocity saturation in high-power semiconductor lasers at ultrahigh drive currents," IEEE Trans. Electron Devices **67**, 4977–4982 (2020).
26. W. Gao, X. Wang, R. Chen, D. B. Eason, G. Strasser, J. P. Bird, and J. Kono, "Electroluminescence from GaAs/AlGaAs heterostructures in strong in-plane electric fields: evidence for k- and real-space charge transfer," ACS Photon. **2**, 1155–1159 (2015).
27. S. O. Slipchenko, O. S. Soboleva, and N. A. Pikhtin, "Unipolar quantum well InGaAs/AlGaAs heterostructures with impact ionization for efficient low-voltage light-emitting devices," IEEE Trans. Electron Devices **68**, 2823–2828 (2021).
28. T. A. Growden, W. Zhang, E. R. Brown, D. F. Storm, D. J. Meyer, and P. R. Berger, "Near-UV electroluminescence in unipolar-doped, bipolar-tunneling GaN/AlN heterostructures," Light Sci. Appl. **7**, 17150 (2018).
29. J. Faist, F. Capasso, D. L. Sivco, C. Sirtori, A. L. Hutchinson, and A. Y. Cho, "Quantum cascade laser," Science **264**, 553–556 (1994).
30. P. Fakhimi, W.-D. Zhang, T. A. Growden, E. R. Brown, R. Droopad, K. M. Hansen, and P. R. Berger, "New device physics of cross-gap electroluminescence in unipolar-doped InGaAs/AlAs RTDs," in *Device Research Conference (DRC)* (2019), pp. 119–120.
31. E. R. Brown, W.-D. Zhang, P. Fakhimi, T. A. Growden, and P. R. Berger, "RTD light emission around 1550 nm with IQE up to 6% at 300 K," in *Device Research Conference (DRC)* (2020), pp. 1–2.
32. F. Hartmann, A. Pfenning, M. Rebello Sousa Dias, F. Langer, S. Höfling, M. Kamp, L. Worschech, L. K. Castelano, G. E. Marques, and V. Lopez-Richard, "Temperature tuning from direct to inverted bistable electroluminescence in resonant tunneling diodes," J. Appl. Phys. **122**, 154502 (2017).
33. E. R. Brown, W.-D. Zhang, T. A. Growden, P. Fakhimi, and P. R. Berger, "Electroluminescence in unipolar-doped $In_{0.53}Ga_{0.47}As$/AlAs resonant-tunneling diodes: a competition between interband tunneling and impact ionization," Phys. Rev. Appl. **16**, 054008 (2021).
34. E. R. C. de Oliveira, A. Pfenning, E. D. G. Castro, M. D. Teodoro, E. C. dos Santos, V. Lopez-Richard, G. E. Marques, L. Worschech, F. Hartmann, and S. Höfling, "Electroluminescence on-off ratio control of *n-i-n* GaAs/AlGaAs-based resonant tunneling structures," Phys. Rev. B **98**, 075302 (2018).
35. C. R. H. White, M. S. Skolnick, L. Eaves, and M. L. Leadbeater, "Electroluminescence and impact ionization phenomena in a double-barrier resonant tunneling structure," Appl. Phys. Lett. **58**, 1164–1166 (1991).
36. E. R. de Oliveira, A. Naranjo, A. Pfenning, V. Lopez-Richard, G. E. Marques, L. Worschech, F. Hartmann, S. Höfling, and M. D. Teodoro, "Determination of carrier density and dynamics via magnetoelectroluminescence spectroscopy in resonant-tunneling diodes," Phys. Rev. Appl. **15**, 014042 (2021).
37. E. D. Guarin Castro, A. Pfenning, F. Hartmann, G. Knebl, M. Daldin Teodoro, G. E. Marques, S. Höfling, G. Bastard, and V. Lopez-Richard, "Optical mapping of nonequilibrium charge carriers," J. Phys. Chem. C **125**, 14741–14750 (2021).
38. B. Jacob, F. Camarneiro, J. Borme, O. Bondarchuk, J. B. Nieder, and B. Romeira, "Surface passivation of III–V GaAs nanopillars by low-frequency plasma deposition of silicon nitride for active nanophotonic devices," ACS Appl. Electron. Mater. **4**, 3399–3410 (2022).
39. F. Hartmann, F. Langer, D. Bisping, A. Musterer, S. Höfling, M. Kamp, A. Forchel, and L. Worschech, "GaAs/AlGaAs resonant tunneling diodes with a GaInNAs absorption layer for telecommunication light sensing," Appl. Phys. Lett. **100**, 172113 (2012).
40. J. C. Blakesley, P. See, A. J. Shields, B. E. Kardynał, P. Atkinson, I. Farrer, and D. A. Ritchie, "Efficient single photon detection by quantum dot resonant tunneling diodes," Phys. Rev. Lett. **94**, 067401 (2005).
41. B. Romeira, J. M. L. Figueiredo, and J. Javaloyes, "NanoLEDs for energy-efficient and gigahertz-speed spike-based sub-λ neuromorphic nanophotonic computing," Nanophotonics **9**, 4149–4162 (2020).

42. B. Romeira, J. Javaloyes, C. N. Ironside, J. M. L. Figueiredo, S. Balle, and O. Piro, "Excitability and optical pulse generation in semiconductor lasers driven by resonant tunneling diode photo-detectors," Opt. Express **21**, 20931–20940 (2013).
43. P. J. Parbrook, B. Corbett, J. Han, T.-Y. Seong, and H. Amano, "Micro-light emitting diode: from chips to applications," Laser Photon. Rev. **15**, 2000133 (2021).
44. D.-H. Kim, Y. S. Park, D. Kang, K.-K. Kim, T.-Y. Seong, and H. Amano, "Combined effects of V pits and chip size on the electrical and optical properties of green InGaN-based light-emitting diodes," J. Alloys Compd. **796**, 146–152 (2019).
45. D.-P. Han, C.-H. Oh, D.-G. Zheng, H. Kim, J.-I. Shim, K.-S. Kim, and D.-S. Shin, "Analysis of nonradiative recombination mechanisms and their impacts on the device performance of InGaN/GaN light-emitting diodes," Jpn. J. Appl. Phys. **54**, 02BA01 (2014).
46. A. Higuera-Rodriguez, B. Romeira, S. Birindelli, L. E. Black, E. Smalbrugge, P. J. van Veldhoven, W. M. M. Kessels, M. K. Smit, and A. Fiore, "Ultralow surface recombination velocity in passivated InGaAs/InP nanopillars," Nano Lett. **17**, 2627–2633 (2017).
47. B. Romeira, J. Borme, H. Fonseca, J. Gaspar, and J. B. Nieder, "Efficient light extraction in subwavelength GaAs/AlGaAs nanopillars for nanoscale light-emitting devices," Opt. Express **28**, 32302–32315 (2020).
48. E. F. Schubert, *Light-Emitting Diodes*, 3rd ed. (E. Fred Schubert, 2018).